ACS APPLIED ENERGY MATERIALS

www.acsaem.org Article

Multifunctional Irradiation-Induced Defects for Enhancing Thermoelectric Properties of Scandium Nitride Thin Films

Dheemahi Rao, Ongira Chowdhury, Ashalatha Indiradevi Kamalasanan Pillai, Gopal K. Pradhan, Satyaprakash Sahoo, Joseph Patrick Feser, Magnus Garbrecht, and Bivas Saha*

Cite This: https://doi.org/10.1021/acsaem.2c00485 Read Online

ACCESS | Metrics & More | Article Recommendations | Supporting Information

ABSTRACT: Scandium nitride (ScN) is an emerging rocksalt indirect bandgap semiconductor with the potential to overcome some of the limitations of traditional wurtzite III (A)-nitride semiconductors in next-generation optoelectronic and thermoelectric applications. Epitaxial ScN thin films contain point defects such as oxygen impurities that result in a high carrier concentration and help achieve a high thermoelectric power factor. However, due to its high thermal conductivity, the thermoelectric figure-of-merit (zT) of ScN is relatively low. Recent theoretical calculations have suggested that scandium and nitrogen vacancies in ScN introduce asymmetric states close to the Fermi energy, increasing its Seebeck coefficient. Increased phonon scattering by these native defects should also reduce thermal conductivity to help achieve higher zT. However, incorporating such native defects in as-deposited ScN is challenging due to their high formation energies. In this work, we introduce native defects in molecular beam epitaxy (MBE)-deposited ScN thin films by lithium-ion irradiation and study the impact of such native defects on ScN's thermoelectric properties. Consistent with theoretical calculations, we find that the Seebeck coefficient in irradiated ScN thin films increases significantly. Thermal conductivity decreases by more than half to 7 ± 1 W/(m·K) at room temperature due to phonon scattering by the irradiation-induced defects. Despite a reduced electrical conductivity due to scattering from defects, irradiated ScN thin films exhibit a high power factor ~(1−2) × 10^{-3} W/(m·K^2) in the 300−950 K range and show a modest increase in the overall zT. This work highlights the multifunctionality of irradiation-induced defects in engineering thermoelectric properties of transition metal nitride semiconductors.

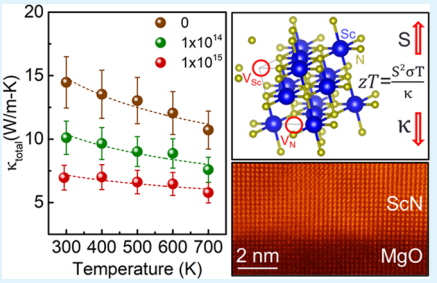

KEYWORDS: *thermoelectricity, defect engineering, III-nitride semiconductors, scandium nitride, ion irradiation, irradiation-induced defects, molecular beam epitaxy*

Downloaded via JAWAHARLAL NEHRU CTR on May 21, 2022 at 05:56:22 (UTC).
See https://pubs.acs.org/sharingguidelines for options on how to legitimately share published articles.

1. INTRODUCTION

Traditional group-III nitride semiconductors such as GaN, AlN, InN, and their solid-solution alloys have revolutionized modern optoelectronic and power-electronic device technologies for over two decades.[1,2] High-quantum yield for light emission, tunable and large band gap, and high breakdown voltage make wurtzite nitride semiconductors attractive for applications in solid-state lighting, optical communication, photodetectors, sensors, and many other fields.[3−5] However, for several emerging applications such as thermoelectrics, plasmonics, and brain-inspired artificial synapses, group-III (A) nitride semiconductors are not well suited. For example, achieving a high thermoelectric figure-of-merit (zT) for waste-heat recovery and cooling requires materials to exhibit ultralow thermal conductivity, which wurtzite nitride semiconductors do not show.[6−8] Similarly, the achievement of high-quality plasmon resonance requires high carrier concentration (>10^{20} cm^{-3}) and high mobility that is not always possible to achieve with traditional nitride semiconductors.[9] Scandium nitride (ScN), a group-III (B) transition metal nitride (TMN), can overcome most of the limitations of group-III (A) nitride semiconductors for a variety of applications.[10,11] ScN exhibits a rocksalt crystal structure with octahedral bonding coordination and, like most other TMNs, shows a high melting temperature (2600 °C), corrosion resistance, high hardness, and structural and morphological stability at ambient conditions.[12−14] Absorption studies have shown that marking a departure from the direct bandgap group-III (A) nitrides, ScN exhibits an indirect Γ−X band gap of ~0.9 eV and a direct Γ−Γ band gap of 2.2 eV.[15−17] Such a crystal structure, bonding coordination, and electronic properties make ScN attractive for several emerging applications.

Since ScN(111) is lattice-matched with GaN(0001), ScN interlayers have been extensively researched to reduce dislocation densities in GaN epilayers.[18,19] As metallic TMNs

Received: February 14, 2022
Accepted: May 9, 2022

© XXXX American Chemical Society

(such as TiN, ZrN, HfN) exhibit the same rocksalt crystal structure and similar lattice parameters as ScN, epitaxial (Zr,Hf)N/ScN metal/semiconductor superlattices are developed for thermionic emission applications.[20−24] Wurtzite $Al_{1-x}Sc_xN$ exhibits a high *c*-axis piezoelectric coefficient and is actively researched for engineering bulk and surface acoustic devices.[25] However, due to its promising thermoelectric properties, ScN is much desired in recent times. The ScN thin films exhibit a high thermoelectric power factor of (2−3.5) × 10^{-3} W/(m·K^2) in the 600−840 K temperature range that is higher than the power factor of most well-established thermoelectric materials such as Bi_2Te_3, Bi_2Se_3, and PbTe.[26−32] Such a high power factor in ScN arises from its high electron concentration in the (1−5) × 10^{20} cm^{-3} range due to the presence of unwanted impurities such as oxygen and possible nitrogen vacancies.[33−35] Molecular beam epitaxy (MBE) and sputter-deposited ScN films also exhibit moderately large mobility in the 90−120 $cm^2/(V·s)$ range.[26,36] However, the highest mobility of 284 $cm^2/(V·s)$ is reported in hybrid vapor phase epitaxy (HVPE)-deposited ScN films.[37] Mg−hole doping has been used recently to reduce the carrier concentration in ScN, and p-type ScN films with a large Seebeck coefficient are demonstrated.[38,39] X-ray absorption spectroscopy (XAS), X-ray photoelectron spectroscopy (XPS), and ultraviolet photoemission spectroscopy (UPS) measurements have shown that both the unwanted n-type oxygen impurity and p-type Mg−hole doping do not introduce defect states inside the band gap, and the rigid band electronic structure remains unchanged with respect to the dopant introduction.[40,41]

Despite the large power factor, the overall zT of ScN is relatively low at 0.17−0.30 in the 500−840 K temperature range due to its high thermal conductivity of ∼12−14 W/(m·K) at room temperature and 8.34 W/(m·K) at 800 K.[23,25,38] Efforts to reduce the thermal conductivity with solid-state alloying of ScN with other heavy metals such as niobium (Nb) and chromium (Cr) have been made. Thermal conductivity decreases to as low as 2.2 and 2.3 W/(m·K) at room temperature for $Sc_{1-x}Nb_xN$ and $Sc_{1-x}Cr_xN$, respectively, due to the phonon scattering alloys.[42,43] Similarly, Mg implantation in ScN(111) reduced the thermal conductivity to 3.2 W/(m·K) at room temperature.[44] However, the decrease in thermal conductivity is also accompanied by a reduction in the power factor that leaves the overall zT practically unchanged. Therefore, techniques with which thermal conductivity can be reduced without altering the power factor will be helpful for ScN's thermoelectric applications.

Recent theoretical calculations have shown that introducing native defects such as Sc and N vacancies in ScN should introduce asymmetric peaks close to the Fermi level in the electronic densities of states (DOS).[45] Since asymmetric peaks close to the Fermi level in DOS are proposed to increase the Seebeck coefficient and power factor, defect engineering of ScN could provide ways to improve its thermoelectric properties.[46] The presence of native defects should also scatter short-to-mid wavelength phonon modes, thereby reducing its thermal conductivity, which is necessary for achieving high zT. However, incorporating such native defects (except for nitrogen vacancies) in ScN is challenging as they are thermodynamically not stable and possess very high formation energies. For example, first-principles modeling has shown that the formation energy of a Sc vacancy in ScN is 4 eV when the Fermi level is at the conduction band minimum.[47,48] At the same time, Sc interstitials and Sc in N sites have about 5 eV formation energies.[48] Due to such high formation energies, as-deposited ScN films in MBE or magnetron-sputtering methods with high substrate temperature generally do not contain many native defects.

However, point defects can be incorporated in thin films by irradiation-induced damage, as recently demonstrated for a Bi_2Te_3 film with He-ion irradiation.[49] High-energy-irradiated ions displace atoms from their equilibrium lattice positions and create point defects like vacancies, interstitials, and many types of defect complexes. With this motivation, in this article, we irradiate MBE-deposited nominally single-crystalline ScN thin films with Li ions and study their thermoelectric properties. Our results show that consistent with the theoretical prediction,[45] the irradiation-induced defects in ScN increase the Seebeck coefficient appreciably and, at the same time, decrease the thermal conductivity drastically. However, an increase in the Seebeck coefficient is also accompanied by a decrease in electrical conductivity. The thermoelectric power factor of the irradiated films remains high at ∼(1−2) × 10^{-3} W/(m·K^2) in the 300−950 K range. Further, on annealing the irradiated films, the structural and optical properties are recovered, while the thermoelectric properties are preserved.

2. METHODS

ScN thin films are deposited on MgO(001) substrates using plasma-assisted molecular beam epitaxy (PAMBE). Five single-side polished 1 cm × 1 cm substrates are ultrasonicated in acetone and methanol for 10 min each before loading into the load lock chamber. The substrates are heated at 600 °C for 60 min in a preparation chamber to eliminate the adsorbed impurities. Subsequently, the substrates are transferred into a growth chamber with a base pressure of 5 × 10^{-11} Torr. A scandium K-cell is heated to 1295 °C to obtain a beam equivalent pressure (BEP) of 1 × 10^{-7} Torr. An RF power source with 375 W is used to generate the nitrogen plasma, and the nitrogen flow is set to 1.5 sccm. Substrates are held at 650 °C during all depositions. The films are deposited for 150 min with a growth rate of 2.5 nm/min.

Four of the pristine (intentionally-undoped) ScN films are irradiated with Li ions of 35 keV in a vacuum. The Li-ion beam is incident normally on ScN films at room temperature with a dose of 5 × 10^{13}, 1 × 10^{14}, 5 × 10^{14}, and 1 × 10^{15} ions/cm^2. A pristine ScN thin film without any Li irradiation is used as a reference to study the role of irradiation-induced defects.

The Stopping and Range of Ions in Matter (SRIM) program is used to simulate the Li-atom penetration depth and the irradiation-induced damages in the ScN films.[50] The structural changes induced by irradiation are analyzed using high-resolution X-ray diffraction (HRXRD). Cross-sectional high-angle annular dark-field scanning transmission electron microscopy (HAADF-STEM) images and energy-dispersive X-ray spectroscopy (EDS) mapping are recorded with a monochromated and image- and probe-corrected FEI Themis-Z transmission electron microscope at 300 kV. EDS maps are recorded with count rates of well above 1 million per map, and background correction is performed by k-factor methods and absorption correction. The room temperature Hall measurements are performed with an Ecopia HMS-3000 machine. Linseis LSR-3 is used to measure the thermoelectric properties (Seebeck coefficient, electrical resistivity, and power factor) as a function of temperature in the 400−1000 K range. Optical bandgap changes are studied with the transmittance and the reflectance spectrum obtained from a Perkin-Elmer lambda 750 spectrometer. Finally, temperature-dependent thermal conductivity is measured with a time-domain thermoreflectance (TDTR) method. More details about the growth, irradiation, and characterization techniques are presented in the Supporting Information (SI).

https://doi.org/10.1021/acsaem.2c00485
ACS Appl. Energy Mater. XXXX, XXX, XXX−XXX

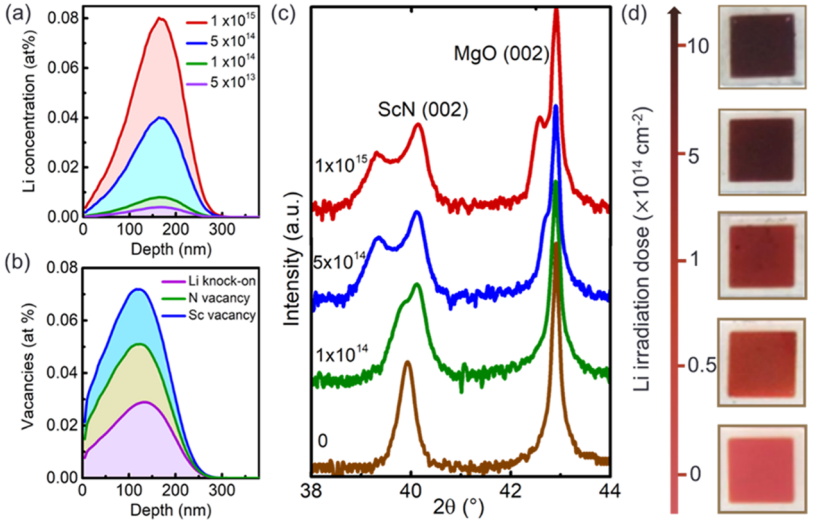

Figure 1. (a) SRIM simulated curves for Li distribution in ScN for different irradiation dosages at 35 keV, (b) simulated concentration of vacancies in ScN created by irradiating 1×10^{15} ions/cm^2 at 35 keV, and (c) offset-separated 2θ-ω scans for ScN(002) deposited on the MgO(001) substrate irradiated with different dosages. The shoulder peaks at lower 2θ become prominent at a higher dosage. (d) Optical images of ScN films showing the visual changes upon irradiation at different dosages, as indicated by the scale on the left.

3. RESULTS AND DISCUSSION

3.1. Structural and Optical Characterization. SRIM simulation (see Figure 1) shows that irradiated Li ions in ScN form a Gaussian pattern with the highest concentration at its peak. The depth of this peak from the surface, termed the projected range, depends on the energy of the irradiated ion beam. For the 35 keV Li beam incident normally to the ScN film, the projected range is calculated to be 150 nm. Beyond 150 nm, the Li concentration tapers off till around 300 nm. So, for the 375 nm thick film studied here, the irradiating ions do not reach the substrate. Figure 1a shows the simulated Li-ion distribution in the ScN film for different irradiation dosages. With increasing irradiation flux, the density of Li atoms at a particular depth increases. The irradiated ions will displace the target atoms, creating vacancies or replacements. Simulation reveals that 96% of the Li will create vacancies in ScN, while only 4% will replace the target atoms. The primary collision of Li ions will create vacancies either by moving the target atoms to interstitial sites or by completely knocking out the atoms from the target. The density of vacancies generated by primary knocks of Li irradiation with 1×10^{15} ions/cm^2 is presented in Figure 1b. The displaced target atoms with sufficient energy will cause secondary collisions and create more vacancies. Figure 1b also shows the total Sc and N vacancies caused by primary and secondary collisions. However, as SRIM calculations are performed at 0 K, it does not consider the annealing of vacancies at room temperature. Therefore, assuming that 99% of the created vacancies will instantly get annealed at the implantation temperature, total vacancies in ScN are calculated to be 0.12 atom % for the flux of 1×10^{15} ions/cm^2. Therefore, this analysis highlights that a significant number of defects are formed in ScN by Li irradiation.

The lattice defects created by ion irradiation are unveiled in the high-resolution X-ray diffraction (HRXRD) (see Figure 1c) analysis. As observed previously, MBE-deposited ScN on a MgO substrate grows epitaxially with (002) orientations with the prominent 002 peak located at a 39.9° 2θ-value. This peak corresponds to a lattice parameter of 4.50 Å that is consistent with previous reports. Due to the smaller lattice constant of 4.21 Å, the MgO peak appears at a 42.9° 2θ-value. This lattice mismatch will cause a compressive strain of about 6% in the initial few layers of ScN. However, the strain will be gradually relaxed by generating dislocations along the growth direction. For a low irradiation dosage, the ScN peak broadens, indicating the strain developed due to implantation. As the dosage increases to 1×10^{14} ions/cm^2 and above, this broadening shows up as a separate shoulder peak shifting to lower 2θ-values and well separating from the 002 ScN peak. This shoulder peak indicates lattice expansion due to the displaced atoms, which mainly leave behind vacancies. The possibility of secondary phase formation by Li irradiation can be excluded as the extra peak is not located at a particular 2θ across the samples, and its intensity does not increase as the Li dosage is increased.

Contrary to the full-width at half-maximum (FWHM) of the rocking curve (ω-scan) corresponding to the 002 peaks of 0.52° for pristine ScN, films irradiated with the highest irradiation dosage of 1×10^{15} ions/cm^2 exhibit an FWHM value of 0.68° that highlight the degradation of structural quality. A similar shoulder peak is also observed in the 002 MgO diffraction spot revealing the damage caused to the substrate by the irradiation. In SRIM simulation, Li ions do not reach the substrate. Therefore, damage to the substrate in the experiment might result from channeling of normal incident Li ions along ScN [002]. Even here, the shoulder peak shifts to lower 2θ at higher irradiation dosages, implying lattice expansion due to significant damage. As discussed in the SI, the 002 peak of ScN in all irradiated films is slightly shifted to higher 2θ values with respect to the pristine ScN due to a small amount of impurity.

The visual changes in the ScN thin film due to the irradiation are shown in Figure 1d. The samples appear darker at higher irradiation dosages, as the reflectivity is reduced by the irradiation-induced damages. The absorption coefficient (α) is calculated from the transmittance (T) and reflectance (R) data using eq 1, where t is the film thickness. Tauc's plot shows bandgap reduction and band edge smearing in the irradiated films. The Urbach energy (E_u) calculated with eq 2 is higher for irradiated films than the pristine ScN, reflecting

https://doi.org/10.1021/acsaem.2c00485
ACS Appl. Energy Mater. XXXX, XXX, XXX−XXX

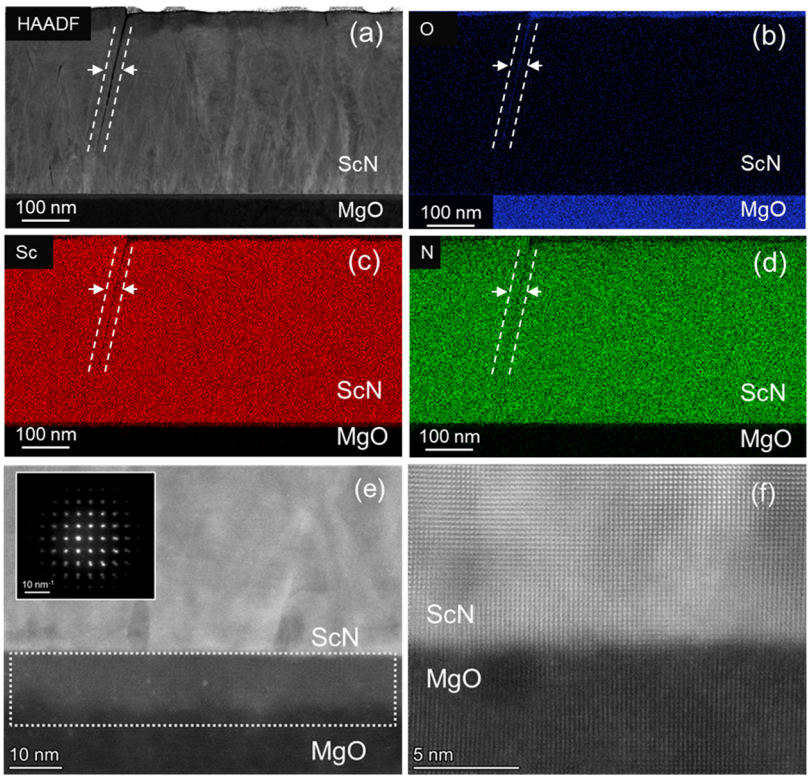

Figure 2. (a) Cross-sectional HAADF-STEM image of the irradiated ScN film deposited on the MgO(001) substrate depicting the compact crystalline film with dislocation and a few diagonal voids separating grains of same orientation (marked with the dashed lines). (b), (c), and (d) show the oxygen (O), scandium (Sc), and nitrogen (N) EDS maps, respectively. Scandium and nitrogen are uniformly distributed in the film, while oxygen is clustered at the void. (e) STEM image of the ScN/MgO interface revealing the damage caused to the substrate (area enclosed within the box) due to channeling of the irradiation ions. The selective area electron diffraction (SAED) pattern in the inset shows that ScN deposited on MgO is cubic and single crystalline. (f) High-resolution image of the sharp ScN/MgO interface with cube-on-cube epitaxy.

Table 1. Room-temperature electron concentration (n), mobility (μ), and resistivity (ρ) of as-deposited ScN thin films (before irradiation) and after irradiation at different dosages.

	before irradiation			after irradiation		
sample	n (cm^{-3})	μ ($cm^2/(V{\cdot}s)$)	ρ (Ω cm)	n (cm^{-3})	μ ($cm^2/(V{\cdot}s)$)	ρ (Ω cm)
0	2.3×10^{20}	60	4.6×10^{-4}			
5×10^{13}	1.99×10^{20}	43	7.3×10^{-4}	1.7×10^{20}	40	8.8×10^{-4}
1×10^{14}	1.85×10^{20}	50	6.8×10^{-4}	1.7×10^{20}	42	8.8×10^{-4}
5×10^{14}	1.87×10^{20}	48	7.0×10^{-4}	1.4×10^{20}	42	1×10^{-3}
1×10^{15}	1.99×10^{20}	40	7.7×10^{-4}	1.3×10^{20}	41	1.2×10^{-3}

the tailing of states at the band edge. A representative Tauc's plot and Urbach energy calculation for ScN irradiated with a flux of 1×10^{15} ions/cm^2 is presented in Figure 5b. The band gap of pristine ScN is 2.2 eV, and it reduces to 2 eV upon irradiation. The Urbach energy increases to 500 meV from 100 meV after irradiation. Hence, the defect formation is evident from optical properties as well.

$$\alpha = \frac{1}{t}\ln\left[\frac{(1-R)}{T}\right] \quad (1)$$

$$\ln \alpha = \ln \alpha_o + \left(\frac{1}{E_u}\right)h\nu \quad (2)$$

The MBE-deposited ScN thin films remain crystalline, smooth, and compact even after the irradiation with a 1×10^{15} ions/cm^2 dosage, as observed in HAADF-STEM images (Figure 2). A few voids are observed in the low-magnification image (Figure 2a) that originate from the lack of adatom mobility during growth and the resultant Ehrlich−Schwoebel barrier, as was discussed in detail previously for ScN films.[51,52] STEM-EDS mapping reveals the uniform distribution of scandium and nitrogen atoms throughout the film and unintentional oxygen incorporation mostly in the voids (Figure 2b−d). Voids are also depleted of scandium and nitrogen atoms. High-resolution images (see Figure 2e) show the compact ScN film, and visible MgO substrate damage (marked by the box) caused due to the channeling of the irradiated ions. This agrees with the shoulder appearing in the 002 MgO peak in HRXRD. The selective area electron diffraction (SAED) pattern in the inset demonstrates the cubic epitaxial growth of the film on the substrate. The atomic-resolution cross-sectional image (Figure 2f) exhibits the cube-on-cube epitaxial growth of ScN on MgO with an epitaxial relationship of (001)[001] ScN || (001)[001] MgO. Microscopy imaging revealed that the irradiation-induced damages do not drastically degrade the crystallinity of ScN films.

https://doi.org/10.1021/acsaem.2c00485
ACS Appl. Energy Mater. XXXX, XXX, XXX−XXX

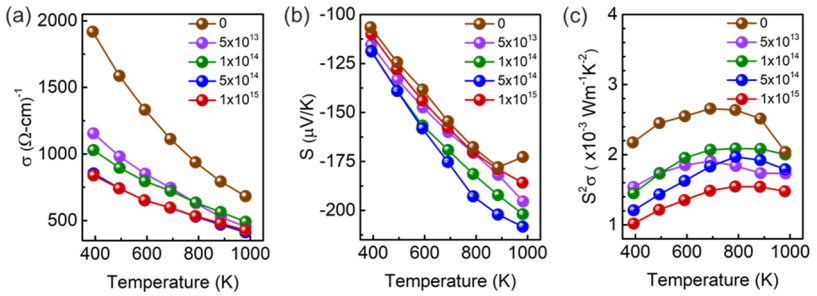

Figure 3. Temperature-dependent (a) electrical conductivity, (b) Seebeck coefficient, and (c) power factor of the pristine and irradiated ScN thin film are presented. Irradiation enhances the Seebeck coefficient to −208 μV/K at 980 K. In spite of the reduction in electrical conductivity, the power factor of irradiated ScN exhibit high values in the range of (1−2) × 10^{-3} W/(m·K^2) within the measured temperature range.

3.2. Electronic and Thermoelectric Characterization.

Hall measurement shows that the room-temperature carrier concentration, mobility, and resistivity of the as-deposited ScN film are about 2 × 10^{20} cm^{-3}, 45 cm^2/(V·s), and 7 × 10^{-4} ohm·cm, respectively. Room-temperature electrical properties of the individual ScN films before and after irradiation are listed in Table 1. Since sample 0 is deposited in the first run, and subsequently all other four films are deposited simultaneously, there is a slight difference in their electrical properties before irradiation. The carrier concentration decreases slightly for higher irradiation dosages and the resistivity increases, perhaps due to the increased scattering. However, it is clear from the table that Li itself, by and large, is electronically inactive in ScN and instead acts as a high-energy source for structural defect formation. The electrical conductivity of the pristine and irradiated films decreases at higher temperatures (see Figure 3a), indicating degenerate-semiconducting behavior due to the high electron concentration. The irradiated films show a lower conductivity than the pristine ScN throughout the measured temperature range. Such temperature deactivation of electrical conductivity is reminiscent of degenerate semiconducting or semimetallic electronic nature of ScN since Fermi energy resides ∼0.1−0.2 eV inside the conduction band edge in ScN.[39] It is important to note that though the irradiation softens such a deactivation process, irradiated ScN still exhibits degenerate semiconductor behavior. Compared to the pristine film, irradiated ScN with the maximum dosage of 1 × 10^{15} ions/cm^2 shows an electrical conductivity decrease by around 62% at room temperature and 40% at 980 K. On the other hand, the absolute value of the Seebeck coefficient of irradiated ScN films is higher than the Seebeck coefficient of pristine ScN and increases with an increase in temperature (see Figure 3b). A maximum Seebeck coefficient of −208 μV/K is found for the ScN film irradiated with a 5 × 10^{14} ions/cm^2 dosage that is ∼12% higher than the Seebeck coefficient of pristine ScN at 980 K. Since the defect concentration is small, the effective mass of carriers is expected to remain unchanged. Hence, the increase in the Seebeck coefficient is primarily due to the appearance of asymmetric peaks in the DOS close to the Fermi energy, as suggested by previous calculations.[45] However, as the carrier concentration of the films reduces slightly due to the irradiation, the increase in the Seebeck coefficient might also have a small contribution from the carrier density reduction.

Despite the high Seebeck coefficients, the overall thermoelectric power factor of all irradiated ScN is smaller than that of the pristine ScN (see Figure 3c). However, all irradiated films exhibit a power factor in the range of (1−2) × 10^{-3} W/(m·K^2) within a 300−1000 K temperature range that in itself is a significantly high value. ScN irradiated with a dosage of 1 × 10^{14} ions/cm^2 exhibits the maximum power factor of ∼2 × 10^{-3} W/(m·K^2) within the 600−950 K temperature range, which is slightly smaller than 2.3 × 10^{-3} W/(m·K^2) for pristine ScN in the same temperature range.

Temperature-dependent thermal conductivity of pristine ScN and films irradiated with a dosage of 1 × 10^{14} and 1 × 10^{15} ions/cm^2 is measured with a TDTR technique. As the electronic contribution to the thermal conductivity ($\kappa_{electron}$) is rather small (see inset of Figure 4), the total thermal

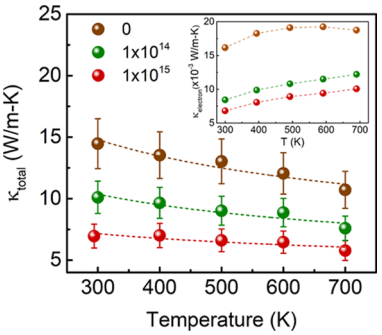

Figure 4. Temperature-dependent thermal conductivity of the pristine and irradiated ScN thin film with two dosages are presented. Irradiation with 1 × 10^{15} ions/cm^2 reduces the thermal conductivity by half to 7 ± 1 W/(m·K) at room temperature. The electronic contribution ($\kappa_{electron}$) to the thermal conductivity is very small at all temperatures as presented in the inset. (dashed lines are guide to the eye).

conductivity (Figure 4) is dominated by the lattice ($\kappa_{lattice}$) contribution that was extracted using the Wiedemann−Franz law. Results show that consistent with the previous reports, the ScN thin film exhibit a high thermal conductivity of ∼14.5 W/(m·K) at room temperature. However, with the irradiation, thermal conductivity decreased drastically to 10 ± 1.3 and 7 ± 1 W/(m·K) at room temperature for the irradiation dosage of 1 × 10^{14} and 1 × 10^{15} ions/cm^2, respectively. Therefore, thermal conductivity is reduced to half of the pristine ScN's value for the film irradiated with the highest irradiation dosage. Such a decrease in thermal conductivity results from the scattering of phonons from the point defects. As $\kappa_{lattice}$ is three orders of magnitude larger than $\kappa_{electron}$, it is evident that reduction in thermal conductivity is dominated by phonon scattering by the irradiation-induced defects. Fitting of the temperature-dependent $\kappa_{lattice}$ with the Umklapp scattering model ($\kappa = AT^{-\alpha}$, where κ, A, T, and α are thermal

https://doi.org/10.1021/acsaem.2c00485
ACS Appl. Energy Mater. XXXX, XXX, XXX−XXX

conductivity, a constant, absolute temperature, and Umklapp scattering exponent, respectively) shows an Umklapp scattering exponent of 0.33, 0.31, and 0.2 for the pristine ScN film and ScN films irradiated with a 1×10^{14} and 1×10^{15} ions/cm^2 dosage, respectively (see SI). Such smaller values of α are a clear sign of the presence of defects.[53,54] With the knowledge of the temperature-dependent power factor and thermal conductivity, the zT for pristine ScN and ScN irradiated with 1×10^{14} ions/cm^2 is calculated to be 0.17 and 0.19 at 700 K (see SI). The slight increase in zT of the irradiated samples with respect to the pristine ScN is within the error bars. The reduction in the thermal conductivity and increase in the Seebeck coefficient in the irradiated ScN films are offset by the reduction in electrical conductivity.

3.3. Annealing of Defects at High Temperature. All irradiated ScN films are heated to 700 °C for 2 min to determine if the irradiation-induced defects in ScN can be annealed at high temperatures. Surface colors of all irradiated ScN films return to pristine ScN's color after the annealing process (see Figure 5a) due to the increased reflection from the surface. Optical absorption measurement shows that the absorption threshold, band gap, and Urbach energy of the irradiated and annealed film become the same as that of the pristine ScN (see Figure 5b). HRXRD also clearly indicates that the extra shoulder 002 peaks at lower 2θ-values disappear after the annealing. The reappearance of the well-defined ScN 002 peak demonstrates the lattice relaxation. Improvement in the crystalline quality can also be observed by a slight decrease in the FWHM of the rocking curve corresponding to the 002 peaks (see Figure 5c) for ScN irradiated with 1×10^{14} ions/cm^2. The Seebeck coefficient and electrical conductivity of irradiated ScN films are preserved after annealing (see SI for details).

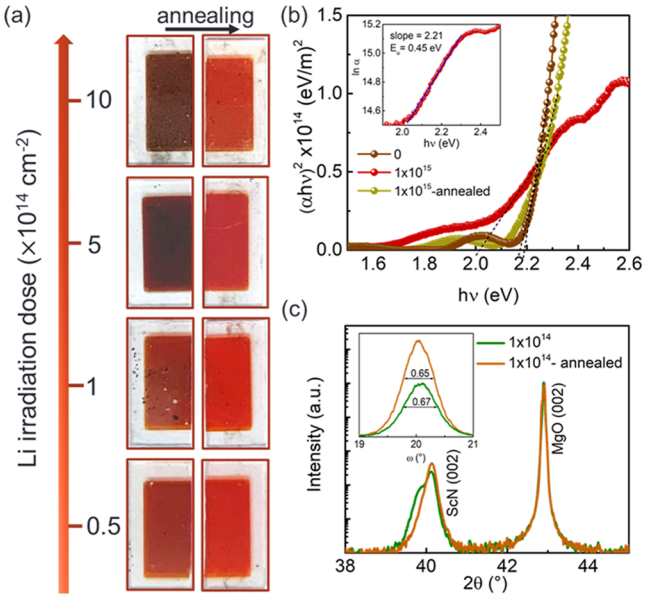

Figure 5. (a) Optical images indicating the color changes of the irradiated ScN films after annealing at 700 °C. (b) Tauc's plot for ScN irradiated with 1×10^{15} ions/cm^2. The reduced band gap and larger smearing in Li-irradiated ScN are reversed on heating. The Urbach energy is calculated from the ln α-vs-$h\nu$ plot shown in the inset. (c) Shoulder peak arising after irradiation of 1×10^{14} ions/cm^2 disappears on heating. The inset shows the reduction in the FWHM of the rocking curve on annealing.

4. CONCLUSIONS

In conclusion, we show that consistent with the theoretical predictions, irradiation-induced defects in ScN thin films increase the Seebeck coefficient and reduce thermal conductivity. Li ions of 35 keV are irradiated on MBE-deposited ScN thin films to create point defects, and HRXRD is used to study them. The defects in ScN expand the lattice and result in a shoulder peak (with broadening) adjacent to the 002 diffraction peak. STEM imaging revealed that even with an irradiation dosage of 1×10^{15} ions/cm^2, ScN maintains its epitaxy and compact crystal structure. The predicted appearance of asymmetric densities of states close to the Fermi energy increases the Seebeck coefficient by more than 12% at all temperatures. Phonon scattering from the irradiation-induced defects also drastically reduces the thermal conduction of ScN by a half. Even with a reduced electrical conductivity, irradiated films exhibit a high power factor in the range of $(1-2) \times 10^{-3}$ W/(m·K^2) within the 300−700 K temperature range. Further, when the irradiated films are annealed, the optical properties are recovered, while the electrical conductivity and the Seebeck coefficient are preserved. Our results show the multifunctionality of irradiation-induced defects for engineering the thermoelectric properties of ScN, which might be applicable to similar material systems.

■ ASSOCIATED CONTENT

Supporting Information

The Supporting Information is available free of charge at https://pubs.acs.org/doi/10.1021/acsaem.2c00485.

Information related to growth, characterization methods, HRXRD and SEM analysis, and TDTR data analysis (PDF)

■ AUTHOR INFORMATION

Corresponding Author

Bivas Saha − *Chemistry and Physics of Materials Unit, Jawaharlal Nehru Centre for Advanced Scientific Research, Bangalore 560064, India; International Centre for Materials Science and School of Advanced Materials (SAMat), Jawaharlal Nehru Centre for Advanced Scientific Research, Bangalore 560064, India;* orcid.org/0000-0002-0837-1506; Email: bsaha@jncasr.ac.in, bivas.mat@gmail.com

Authors

Dheemahi Rao − *Chemistry and Physics of Materials Unit, Jawaharlal Nehru Centre for Advanced Scientific Research, Bangalore 560064, India; International Centre for Materials Science, Jawaharlal Nehru Centre for Advanced Scientific Research, Bangalore 560064, India*

Ongira Chowdhury − *Department of Mechanical Engineering, University of Delaware, Newark, Delaware 19716, United States;* orcid.org/0000-0003-0853-2223

Ashalatha Indiradevi Kamalasanan Pillai − *Australian Centre for Microscopy and Microanalysis, The University of Sydney, Camperdown, NSW 2006, Australia*

Gopal K. Pradhan − *Department of Physics, School of Applied Sciences, KIIT Deemed to be University, Bhubaneswar 751024 Odisha, India;* orcid.org/0000-0002-1956-7248

https://doi.org/10.1021/acsaem.2c00485
ACS Appl. Energy Mater. XXXX, XXX, XXX−XXX

Satyaprakash Sahoo − *Laboratory for Low Dimensional Materials, Institute of Physics, Bhubaneswar 751005, India; Homi Bhabha National Institute, Mumbai 400094, India;* orcid.org/0000-0001-9766-3713

Joseph Patrick Feser − *Department of Mechanical Engineering, University of Delaware, Newark, Delaware 19716, United States;* orcid.org/0000-0001-9918-3844

Magnus Garbrecht − *Australian Centre for Microscopy and Microanalysis, The University of Sydney, Camperdown, NSW 2006, Australia*

Complete contact information is available at: https://pubs.acs.org/10.1021/acsaem.2c00485

Notes

The authors declare no competing financial interest.

■ ACKNOWLEDGMENTS

D.R. and B.S. acknowledge International Center for Materials Science (ICMS) and Sheikh Saqr Laboratory (SSL) in JNCASR for support. B.S. acknowledges the Science and Engineering Research Board (SERB) of the Government of India, Start-Up Research grant SRG/2019/000613, for financial support. G.K.P. and S.S. acknowledge Science and Engineering Research Board (SERB) of the Government of India, Core Research grant CRG/2020/006190, for financial support. M.G. and A.I.K.P. acknowledge the facilities of Sydney Microscopy and Microanalysis at the University of Sydney. Help of R. Dash of Ion Beam Laboratory, Institute of Physics, Bhubaneswar, in carrying out the Li-ion implantations is greatly appreciated.

■ REFERENCES

(1) Flack, T. J.; Pushpakaran, B. N.; Bayne, S. B. GaN Technology for Power Electronic Applications: A Review. *J. Electron. Mater.* **2016**, *45*, 2673−2682.

(2) Strite, S.; Morkoc, H. GaN, AlN, and InN: A Review. *J. Vac. Sci. Technol., B* **1992**, *10*, 1237−1266.

(3) Kour, R.; Arya, S.; Verma, S.; Singh, A.; Mahajan, P.; Khosla, A. Review—Recent Advances and Challenges in Indium Gallium Nitride (In x Ga 1-x N) Materials for Solid State Lighting. *ECS J. Solid State Sci. Technol.* **2020**, *9*, No. 015011.

(4) Jiang, Z.; Atalla, M. R. M.; You, G.; Wang, L.; Li, X.; Liu, J.; Elahi, A. M.; Wei, L.; Xu, J. Monolithic Integration of Nitride Light Emitting Diodes and Photodetectors for Bi-Directional Optical Communication. *Opt. Lett.* **2014**, *39*, No. 5657.

(5) Hickman, A. L.; Chaudhuri, R.; Bader, S. J.; Nomoto, K.; Li, L.; Hwang, J. C. M.; Grace Xing, H.; Jena, D. Next Generation Electronics on the Ultrawide-Bandgap Aluminum Nitride Platform. *Semicond. Sci. Technol.* **2021**, *36*, No. 044001.

(6) Zou, J.; Kotchetkov, D.; Balandin, A. A.; Florescu, D. I.; Pollak, F. H. Thermal Conductivity of GaN Films: Effects of Impurities and Dislocations. *J. Appl. Phys.* **2002**, *92*, 2534−2539.

(7) Slack, G. A.; Tanzilli, R. A.; Pohl, R. O.; Vandersande, J. W. The Intrinsic Thermal Conductivity of AIN. *J. Phys. Chem. Solids* **1987**, *48*, 641−647.

(8) Morelli, D. T.; Heremans, J. P. Thermal Conductivity of Germanium, Silicon, and Carbon Nitrides. *Appl. Phys. Lett.* **2002**, *81*, 5126−5128.

(9) Naik, G. V.; Shalaev, V. M.; Boltasseva, A. Alternative Plasmonic Materials: Beyond Gold and Silver. *Adv. Mater.* **2013**, *25*, 3264−3294.

(10) Eklund, P.; Kerdsongpanya, S.; Alling, B. Transition-Metal-Nitride-Based Thin Films as Novel Energy Harvesting Materials. *J. Mater. Chem. C* **2016**, *4*, 3905−3914.

(11) Shakouri, A. Recent Developments in Semiconductor Thermoelectric Physics and Materials. *Annu. Rev. Mater. Res.* **2011**, *41*, 399−431.

(12) Dismukes, J. P.; Yim, W. M.; Ban, V. S. Epitaxial Growth and Properties of Semiconducting ScN. *J. Cryst. Growth* **1972**, *13−14*, 365−370.

(13) Biswas, B.; Saha, B. Development of Semiconducting ScN. *Phys. Rev. Mater.* **2019**, *3*, No. 020301.

(14) Feng, W.; Cui, S.; Hu, H.; Zhang, G.; Lv, Z.; Gong, Z. Phase Stability Electronic and Elastic Properties of ScN. *Phys. B* **2010**, *405*, 2599−2603.

(15) Saha, B.; Acharya, J.; Sands, T. D.; Waghmare, U. V. Electronic Structure, Phonons, and Thermal Properties of ScN, ZrN, and HfN: A First-Principles Study. *J. Appl. Phys.* **2010**, *107*, No. 033715.

(16) Bai, X.; Kordesch, M. E. Structure and Optical Properties of ScN Thin Films. *Appl. Surf. Sci.* **2001**, *175−176*, 499−504.

(17) Al-Brithen, H. A.; Smith, A. R.; Gall, D. Surface and Bulk Electronic Structure of ScN(001) Investigated by Scanning Tunneling Microscopy/Spectroscopy and Optical Absorption Spectroscopy. *Phys. Rev. B* **2004**, *70*, No. 045303.

(18) Moram, M. A.; Zhang, Y.; Kappers, M. J.; Barber, Z. H.; Humphreys, C. J. Dislocation Reduction in Gallium Nitride Films Using Scandium Nitride Interlayers. *Appl. Phys. Lett.* **2007**, *91*, No. 152101.

(19) Acharya, S.; Chatterjee, A.; Bhatia, V.; Pillai, A. I. K.; Garbrecht, M.; Saha, B. Twinned Growth of ScN Thin Films on Lattice-Matched GaN Substrates. *Mater. Res. Bull.* **2021**, *143*, No. 111443.

(20) Rawat, V.; Koh, Y. K.; Cahill, D. G.; Sands, T. D. Thermal Conductivity of (Zr,W)N/ScN Metal/Semiconductor Multilayers and Superlattices. *J. Appl. Phys.* **2009**, *105*, No. 024909.

(21) Saha, B.; Sands, T. D.; Waghmare, U. V. Thermoelectric Properties of HfN/ScN Metal/Semiconductor Superlattices: A First-Principles Study. *J. Phys.: Condens. Matter* **2012**, *24*, No. 415303.

(22) Zebarjadi, M.; Bian, Z.; Singh, R.; Shakouri, A.; Wortman, R.; Rawat, V.; Sands, T. Thermoelectric Transport in a ZrN/ScN Superlattice. *J. Electron. Mater.* **2009**, *38*, 960−963.

(23) Garbrecht, M.; Schroeder, J. L.; Hultman, L.; Birch, J.; Saha, B.; Sands, T. D. Microstructural Evolution and Thermal Stability of HfN/ScN, ZrN/ScN, and Hf0.5Zr0.5N/ScN Metal/Semiconductor Superlattices. *J. Mater. Sci.* **2016**, *51*, 8250−8258.

(24) Garbrecht, M.; McCarroll, I.; Yang, L.; Bhatia, V.; Biswas, B.; Rao, D.; Cairney, J. M.; Saha, B. Thermally Stable Epitaxial ZrN/Carrier-Compensated Sc0.99Mg0.01N Metal/Semiconductor Multilayers for Thermionic Energy Conversion. *J. Mater. Sci.* **2020**, *55*, 1592−1602.

(25) Matloub, R.; Hadad, M.; Mazzalai, A.; Chidambaram, N.; Moulard, G.; Sandu, C. S.; Metzger, T.; Muralt, P. Piezoelectric $Al_{1-x}Sc_xN$ Thin Films: A Semiconductor Compatible Solution for Mechanical Energy Harvesting and Sensors. *Appl. Phys. Lett.* **2013**, *102*, No. 152903.

(26) Rao, D.; Biswas, B.; Flores, E.; Chatterjee, A.; Garbrecht, M.; Koh, Y. R.; Bhatia, V.; Pillai, A. I. K.; Hopkins, P. E.; Martin-Gonzalez, M.; Saha, B. High Mobility and High Thermoelectric Power Factor in Epitaxial ScN Thin Films Deposited with Plasma-Assisted Molecular Beam Epitaxy. *Appl. Phys. Lett.* **2020**, *116*, No. 152103.

(27) Burmistrova, P. V.; Maassen, J.; Favaloro, T.; Saha, B.; Salamat, S.; Rui Koh, Y.; Lundstrom, M. S.; Shakouri, A.; Sands, T. D. Thermoelectric Properties of Epitaxial ScN Films Deposited by Reactive Magnetron Sputtering onto MgO(001) Substrates. *J. Appl. Phys.* **2013**, *113*, No. 153704.

(28) Kerdsongpanya, S.; Van Nong, N.; Pryds, N.; Žukauskaite, A.; Jensen, J.; Birch, J.; Lu, J.; Hultman, L.; Wingqvist, G.; Eklund, P. Anomalously High Thermoelectric Power Factor in Epitaxial ScN Thin Films. *Appl. Phys. Lett.* **2011**, *99*, No. 232113.

(29) Le Febvrier, A.; Tureson, N.; Stilkerich, N.; Greczynski, G.; Eklund, P. Effect of Impurities on Morphology, Growth Mode, and Thermoelectric Properties of (1 1 1) and (0 0 1) Epitaxial-like ScN Films. *J. Phys. D: Appl. Phys.* **2019**, *52*, No. 035302.

(30) Ruiz-Clavijo, A.; Caballero-Calero, O.; Manzano, C. V.; Maeder, X.; Beardo, A.; Cartoixà, X.; Álvarez, F. X.; Martín-González, M. 3D Bi 2 Te 3 Interconnected Nanowire Networks to Increase Thermoelectric Efficiency. *ACS Appl. Energy Mater.* **2021**, *4*, 13556−13566.
(31) Cermak, P.; Knotek, P.; Ruleova, P.; Holy, V.; Palka, K.; Kucek, V.; Benes, L.; Navratil, J.; Drasar, C. High Power Factor and Mobility of Single Crystals of Bi2Se3 Induced by Mo Doping. *J. Solid State Chem.* **2019**, *277*, 819−827.
(32) Paul, B.; Banerji, P. Enhancement in Thermoelectric Power in Lead Telluride Nanocomposite: Role of Oxygen VIS-A-VIS Nanostruct. *J. Nano- Electron. Phys.* **2011**, *3*, 691−697.
(33) More-Chevalier, J.; Cichoň, S.; Horák, L.; Bulíř, J.; Hubík, P.; Gedeonová, Z.; Fekete, L.; Poupon, M.; Lančok, J. Correlation between Crystallization and Oxidation Process of ScN Films Exposed to Air. *Appl. Surf. Sci.* **2020**, *515*, No. 145968.
(34) Cetnar, J. S.; Reed, A. N.; Badescu, S. C.; Vangala, S.; Smith, H. A.; Look, D. C. Electronic Transport in Degenerate (100) Scandium Nitride Thin Films on Magnesium Oxide Substrates. *Appl. Phys. Lett.* **2018**, *113*, No. 192104.
(35) More-Chevalier, J.; Horák, L.; Cichon, S.; Hruškaa, P.; Cížek, J.; Liedke, M. O.; Butterling, M.; Wagner, A.; Bulír, J.; Hubík, P.; Gedeonová, Z.; Lancok, J. Positron Structural Analysis of ScN Films Deposited on MgO Substrate. *Acta Phys. Pol. A* **2020**, *137*, 209−214.
(36) Burmistrova, P. V.; Zakharov, D.; Favaloro, T.; Mohammed, A.; Stach, E.; Shakouri, A.; Sands, T. Effect of Deposition Pressure on the Microstructure and Thermoelectric Properties of Epitaxial ScN(001) Thin Films Sputtered onto MgO(001) Substrates. *J. Mater. Res.* **2015**, *30*, 626−634.
(37) Oshima, Y.; Villora, E. G.; Shimamura, K. Hydride Vapor Phase Epitaxy and Characterization of High-Quality ScN Epilayers. *J. Appl. Phys.* **2014**, *115*, No. 153508.
(38) Saha, B.; Garbrecht, M.; Perez-Taborda, J. A.; Fawey, M. H.; Koh, Y. R.; Shakouri, A.; Martin-Gonzalez, M.; Hultman, L.; Sands, T. D. Compensation of Native Donor Doping in ScN: Carrier Concentration Control and p-Type ScN. *Appl. Phys. Lett.* **2017**, *110*, No. 252104.
(39) Saha, B.; Perez-Taborda, J. A.; Bahk, J.-H.; Koh, Y. R.; Shakouri, A.; Martin-Gonzalez, M.; Sands, T. D. Temperature-Dependent Thermal and Thermoelectric Properties of n-Type and p-Type $Sc_{1-x}Mg_xN$. *Phys. Rev. B* **2018**, *97*, No. 085301.
(40) Nayak, S.; Baral, M.; Gupta, M.; Singh, J.; Garbrecht, M.; Ganguli, T.; Shivaprasad, S. M.; Saha, B. Rigid-Band Electronic Structure of Scandium Nitride across the n-Type to p-Type Carrier Transition Regime. *Phys. Rev. B* **2019**, *99*, No. 161117.
(41) Haseman, M. S.; Noesges, B. A.; Shields, S.; Cetnar, J. S.; Reed, A. N.; Al-Atabi, H. A.; Edgar, J. H.; Brillson, L. J. Cathodoluminescence and X-Ray Photoelectron Spectroscopy of ScN: Dopant, Defects, and Band Structure. *APL Mater.* **2020**, *8*, No. 081103.
(42) Tureson, N.; Van Nong, N.; Fournier, D.; Singh, N.; Acharya, S.; Schmidt, S.; Belliard, L.; Soni, A.; Le Febvrier, A.; Eklund, P. Reduction of the Thermal Conductivity of the Thermoelectric Material ScN by Nb Alloying. *J. Appl. Phys.* **2017**, *122*, No. 025116.
(43) Kerdsongpanya, S.; Sun, B.; Eriksson, F.; Jensen, J.; Lu, J.; Koh, Y. K.; Nong, N.; Van; Balke, B.; Alling, B.; Eklund, P. Experimental and Theoretical Investigation of Cr 1-x Sc x N Solid Solutions for Thermoelectrics. *J. Appl. Phys.* **2016**, *120*, No. 215103.
(44) Tureson, N.; Marteau, M.; Cabioch, T.; Van Nong, N.; Jensen, J.; Lu, J.; Greczynski, G.; Fournier, D.; Singh, N.; Soni, A.; Belliard, L.; Eklund, P.; Le Febvrier, A. Effect of Ion-Implantation-Induced Defects and Mg Dopants on the Thermoelectric Properties of ScN. *Phys. Rev. B* **2018**, *98*, No. 205307.
(45) Kerdsongpanya, S.; Alling, B.; Eklund, P. Effect of Point Defects on the Electronic Density of States of ScN Studied by First-Principles Calculations and Implications for Thermoelectric Properties. *Phys. Rev. B* **2012**, *86*, No. 195140.
(46) Mahan, G. D.; Sofo, J. O. The Best Thermoelectric. *Proc. Natl. Acad. Sci. U.S.A.* **1996**, *93*, 7436−7439.
(47) Balasubramanian, K.; Khare, S. V.; Gall, D. Energetics of Point Defects in Rocksalt Structure Transition Metal Nitrides: Thermodynamic Reasons for Deviations from Stoichiometry. *Acta Mater.* **2018**, *159*, 77−88.
(48) Kumagai, Y.; Tsunoda, N.; Oba, F. Point Defects and P-Type Doping in ScN from First Principles. *Phys. Rev. Appl.* **2018**, *9*, No. 034019.
(49) Suh, J.; Yu, K. M.; Fu, D.; Liu, X.; Yang, F.; Fan, J.; Smith, D. J.; Zhang, Y. H.; Furdyna, J. K.; Dames, C.; Walukiewicz, W.; Wu, J. Simultaneous Enhancement of Electrical Conductivity and Thermopower of Bi2Te3 by Multifunctionality of Native Defects. *Adv. Mater.* **2015**, *27*, 3681−3686.
(50) Ziegler, J. F.; Ziegler, M.-D.; Biersack, J.-P. SRIM—The Stopping and Range of Ions in Matter (2010). *Nucl. Instrum. Methods Phys. Res., Sect. B* **2010**, *268*, 1818−1823.
(51) Garbrecht, M.; Hultman, L.; Fawey, M. H.; Sands, T. D.; Saha, B. Void-Mediated Coherency-Strain Relaxation and Impediment of Cubic-to-Hexagonal Transformation in Epitaxial Metastable Metal/Semiconductor TiN/A L0.72 S C0.28 N Multilayers. *Phys. Rev. Mater.* **2017**, *1*, No. 033402.
(52) Rao, D.; Biswas, B.; Acharya, S.; Bhatia, V.; Pillai, A. I. K.; Garbrecht, M.; Saha, B. Effects of Adatom Mobility and Ehrlich−Schwoebel Barrier on Heteroepitaxial Growth of Scandium Nitride (ScN) Thin Films. *Appl. Phys. Lett.* **2020**, *117*, No. 212101.
(53) Rounds, R.; Sarkar, B.; Alden, D.; Guo, Q.; Klump, A.; Hartmann, C.; Nagashima, T.; Kirste, R.; Franke, A.; Bickermann, M.; Kumagai, Y.; Sitar, Z.; Collazo, R. The Influence of Point Defects on the Thermal Conductivity of AlN Crystals. *J. Appl. Phys.* **2018**, *123*, No. 185107.
(54) Cahill, D. G.; Braun, P. V.; Chen, G.; Clarke, D. R.; Fan, S.; Goodson, K. E.; Keblinski, P.; King, W. P.; Mahan, G. D.; Majumdar, A.; Maris, H. J.; Phillpot, S. R.; Pop, E.; Shi, L. Nanoscale Thermal Transport. II. 2003−2012. *Appl. Phys. Rev.* **2014**, *1*, No. 011305.

https://doi.org/10.1021/acsaem.2c00485
ACS Appl. Energy Mater. XXXX, XXX, XXX−XXX